Structure and ionic conduction enhancement mechanisms at $CeO_2/SrTiO_3$ heterointerfaces

Bonan Zhu[1,2*], Georg Schusteritsch[1,5], Weiwei Li[3,1*], Wandong Xing[4], Rong Yu[4], Chris J. Pickard[1,5], Judith L. MacManus-Driscoll[1]

1 Department of Materials Science and Metallurgy, University of Cambridge, 27 Charles Babbage Rd., Cambridge, CB3 0FS, U.K.

2 School of Aerospace Engineering, Beijing Institute of Technology, Beijing 100081, China

3 College of Physics, State Key Laboratory of Mechanics and Control for Aerospace Structures, MIIT Key Laboratory of Aerospace Information Materials and Physics, Nanjing University of Aeronautics and Astronautics, Nanjing 211106, China

4 National Center for Electron Microscopy in Beijing, School of Materials Science and Engineering, Key Laboratory of Advanced Materials of Ministry of Education of China, The State Key Laboratory of New Ceramics and Fine Processing, Tsinghua University, Beijing, 100084, China

5 Advanced Institute for Materials Research, Tohoku University, Sendai, Japan

*Email address: bzhu@bit.edu.cn; wl337@nuaa.edu.cn

Abstract

Fluorite-perovskite heterointerfaces garner great interest for enhanced ionic conductivity for application in electronic and energy devices. However, the origin of observed enhanced ionic conductivity as well as the details of the atomic structure at these interfaces remain elusive. Here, systematic, multi-stoichiometry computational searches and experimental investigations are performed to obtain stable and exact atomic structures of interfaces between CeO_2 and $SrTiO_3$-two archetypes of the corresponding structural families. Local reconstructions take place at the interface because of mismatched lattices. TiO_2 terminated $SrTiO_3$ causes a buckled rock salt CeO interface layer to emerge. In contrast, SrO terminated $SrTiO_3$ maintains the fluorite structure at the interface compensated by a partially occupied anion lattice. Moderate enhancement in oxygen diffusion is found along the interface by simulations, yet evidence to support further significant enhancement is lacking. Our findings demonstrate the control of interface termination as an effective pathway to achieve desired device performance.

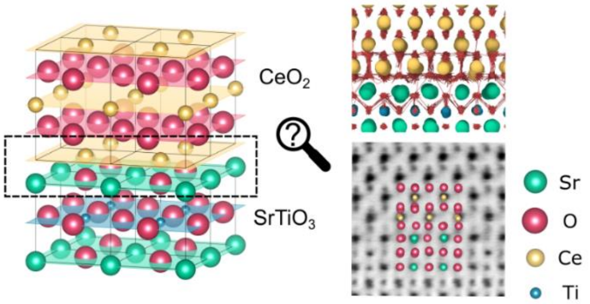

Introduction

Complex oxides exhibit a wide range of phenomena such as superconductivity, ionic conduction, magnetism and multi-ferroelectricity, and they have been intensively studied for applications that include solid oxide fuel cells (SOFCs), batteries, and memory devices[1].[2] In particular, oxide interfaces, like their conventional semiconductor counterparts, offer the unique opportunity to create tuneable novel multifunctionalities by the artificial interfacial modifications, including defects (oxygen or cation vacancies), structural symmetry breaking, interlayer interactions, etc.[3–9] For example, yttria-stabilized zirconia (YSZ) and doped CeO_2 are the materials that have attracted intensive interest in SOFCs because of their chemical compatibility with electrodes and high ionic conductivity.[10,11] In 2008, Garcia-Barriocanal *et al*.[12] reported an eight-orders-of-magnitude enhancement of YSZ conductivity in epitaxial superlattices consisting of 1 nm YSZ and 10 nm $SrTiO_3$ (STO) layers. The colossal enhancement of ionic conductivity was attributed to the combination of the large number of mobile ions together with the expansion of the fluorite structure imposed by the substrate.[13,14] However, these results still need to be independently examined, as there is some debate on whether the observed conductivity of YSZ/STO superlattices is purely ionic.[15–17] The origin of this enhanced ionic conductivity is still unclear, although the effects of strain, substrate, O-sublattice incompatibility, and misfit dislocations at the interface have been explored extensively in related or similar heterointerface systems.[13,18–28]

Direct experimental measurements of interfaces are very challenging since interfaces have small volume fraction and are buried inside the sample. Theoretical and computational approaches can provide valuable insights into interface induced phenomena by idealized yet still realistic atomistic models. Despite many theoretical and computational studies devoted to unravelling the origin of enhanced ionic conductivity at the YSZ/STO interface, only a few studies directly address the possible interface reconstructions at an atomistic level.[29–31] This is due to the difficulty in obtaining interface structures which are essential inputs for any modelling work. State-of-the-art scanning transmission electron microscopy (STEM) can reveal the locations of atomic columns at interfaces, but often cannot give a one-to-one mapping of the full lattice structure. This challenge can be tackled by performing direct computational searches for low energy interface structures. Indeed, recent advances in computational structure prediction algorithms[32–35] have led to discoveries of new high pressure materials[36], defect clusters[37], 2D materials[38] and interfaces.[39,40] Combining both theoretical and experimental structure determination is necessary to get a complete understanding of the interface.

We focus on the CeO_2/STO (001) interface because both CeO_2 and STO are archetypes of their structural families and have technological importance. CeO_2 has the cubic fluorite structure, and it can be tuned to become a high performance ionic conductor through doping with lower valence elements such as Sm and Gd.[41] STO has a cubic perovskite structure and is commercially available as substrates for depositing epitaxial oxide thin films. The (001) CeO_2/STO interfaces studied here can be realized by epitaxial growth of CeO_2 thin films on (001)-oriented STO substrates. Previously, Dyer et al[29] studied the YSZ/STO interface using hand-built models and showed the importance of choosing surface terminations. Ultra-thin ZrO_2/YSZ-STO superlattices have also been studied using interatomic potentials.[30,31] Non-bulk phases were stabilized under both structural mismatch and strain. While YSZ also has the fluorite structure, its smaller lattice constants cause much larger tensile strain when epitaxially grown on STO (7% vs 2%), making it difficult to separate the effects of long ranged biaxial strain and localized interface structural mismatch. In addition, bulk YSZ itself may undergo phase transformation when subjected to strong biaxial tensile strain.[22,42]

In this work, stable and atomic interface structures at (001) CeO_2/STO heterostructures are predicted using *ab initio* Random Structure Searching (AIRSS).[33,43] A collection of low-energy interface structures has been obtained through systematic searching and has been further validated by STEM studies. The interface stoichiometry is found to play an important role in stabilizing the emergent atomic configurations, hence affecting the properties. With SrO terminated STO, the anion sites near the interface become partially occupied, giving rise to enhanced lateral oxygen diffusion up to two orders of magnitudes. On the other hand, structural mismatch at the TiO_2 terminated interface is compensated by a buckled rock salt CeO. In both cases, additional oxygen vacancies are found to be attracted by the interface, which is expected to hinder ionic transport in the perpendicular direction. Overall, interface termination is shown to be an important factor producing interface-induced moderate ionic conductivity enhancement.

Results and Discussion

Finding interface structures

The bulk structures of STO and CeO_2 are both cubic and they share some similarity of atomic arrangements (Figure 1). STO has a cubic perovskite structure of space group $\mathrm{Pm\bar{3}m}$ at room temperature while at low temperatures it turns into an anti-ferrodistortive tetragonal $\mathrm{I4/mcm}$ phase.[44] We limit ourselves to the cubic phase as it is more relevant under growth and application conditions (from room temperature to hundreds of Kelvins). CeO_2 has a cubic structure with $\mathrm{Fm\bar{3}m}$ space group. Cube-on-cube growth takes place when depositing CeO_2 on a STO (001) surface, with the conventional cell of CeO_2 rotated by 45 degrees along the z axis,[45] as depicted in Figure 1a. This gives the CeO_2 an in-plane lattice constant of 3.82 Å, while that of STO is 3.905 Å. Hence, a CeO_2 film is tensile strained by 2% when fully matched to the STO substrate. Such level of strain is reported to slightly enhance the oxygen diffusivity in the bulk structure.[20,46]

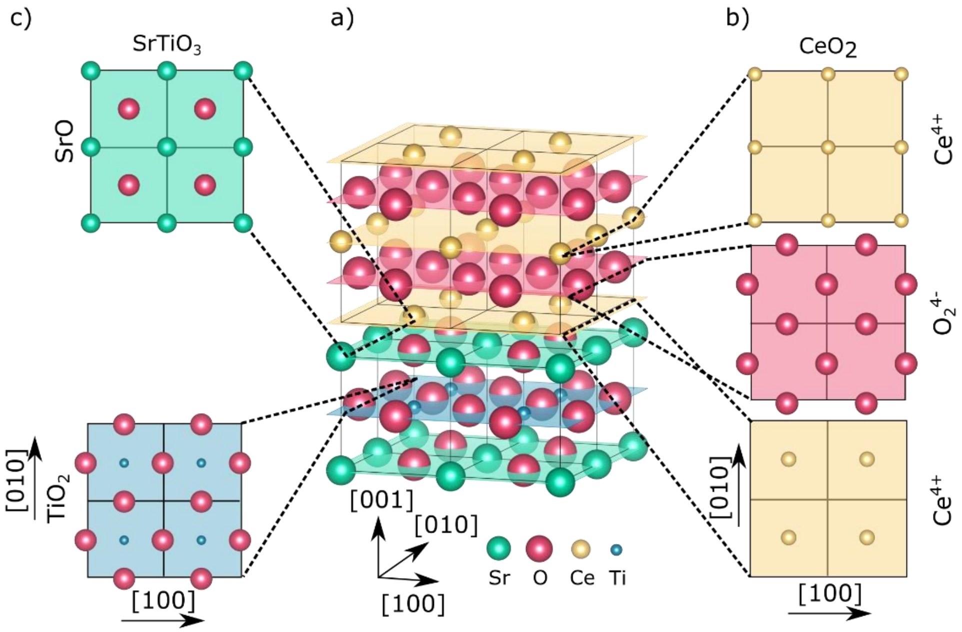

Figure 1. Bulk and interface strucutres. a) Bulk structures of CeO_2 and STO in 3D. b) (001) planes in the CeO_2 film layer, from the interface to the 3rd layer. c) The (001) planes in the STO substrate.

The (001) planes of both STO and CeO_2 are shown in Figure 1b&c. The CeO_2 is consisted of alternating Ce^{4+} (yellow) and O_2^{4-} layers (red). The two adjacent Ce^{4+} layers are inequivalent - one is translated by $0.5\vec{a} + 0.5\vec{b}$ relative to the other, with $\vec{a}$ and $\vec{b}$ being the lattice vectors in the lateral directions. The repeating unit is $Ce_a^{4+} - O_2^{4-} - Ce_b^{4+} - O_2^{4-}$ normal to the interface. Similarly, STO is consisted of alternating SrO and TiO_2 layers (Figure 1). Unlike CeO_2, each layer in STO is charge neutral. Interestingly, the arrangement of oxygen anions in the TiO_2 layer is the same as that in the O_2 layer in CeO_2. The cation sites occupied by Sr and Ti are translated by $0.5\vec{a} + 0.5\vec{b}$ between each layers, similar to that of the Ce layers in CeO_2.

Idealized interface models can be built by stacking blocks of the bulk structures in the [001] direction. There are four possible combinations: "SrO-Ce", "SrO-O_2", "TiO_2-Ce", "TiO_2-O_2". With the lateral alignments limited to three high symmetry arrangements, 12 interface structures can be enumerated. However, these models do not permit reconstructions that may lower the overall energy. In addition, the local stoichiometry at the interface is limited by the use of bulk-like building blocks. Hence, as we will show below, performing variable composition structure searching is essential to acquire a complete picture of the interface and its properties.

Figure 2 shows interface structures obtained via first-principles structure searching. For SrO termination, there are three cases: SrO-Ce, SrO-O_2 and SrO-O. The SrO-Ce case (Figure 2a) does not contain significant reconstruction, although a reduction of the Ce-O interface distance and buckling of the SrO layer can be seen. The lateral alignment of the layers is consistent with the minimization of the electrostatic energy. On the other hand, a significant reconstruction appears in the structure with the SrO-O_2 termination. In Figure 2b, oxygen ions at the interface form O-O bonds with bond lengths between 1.45 Å and 1.50 Å which are similar to that of the peroxide groups. Three peroxide groups are in the SrO layer, and one is in the layer above. The formation of peroxide groups reduces the excessive negative charge at the interface due to O^{2-}. This also mitigates the polar discontinuity at the interface.

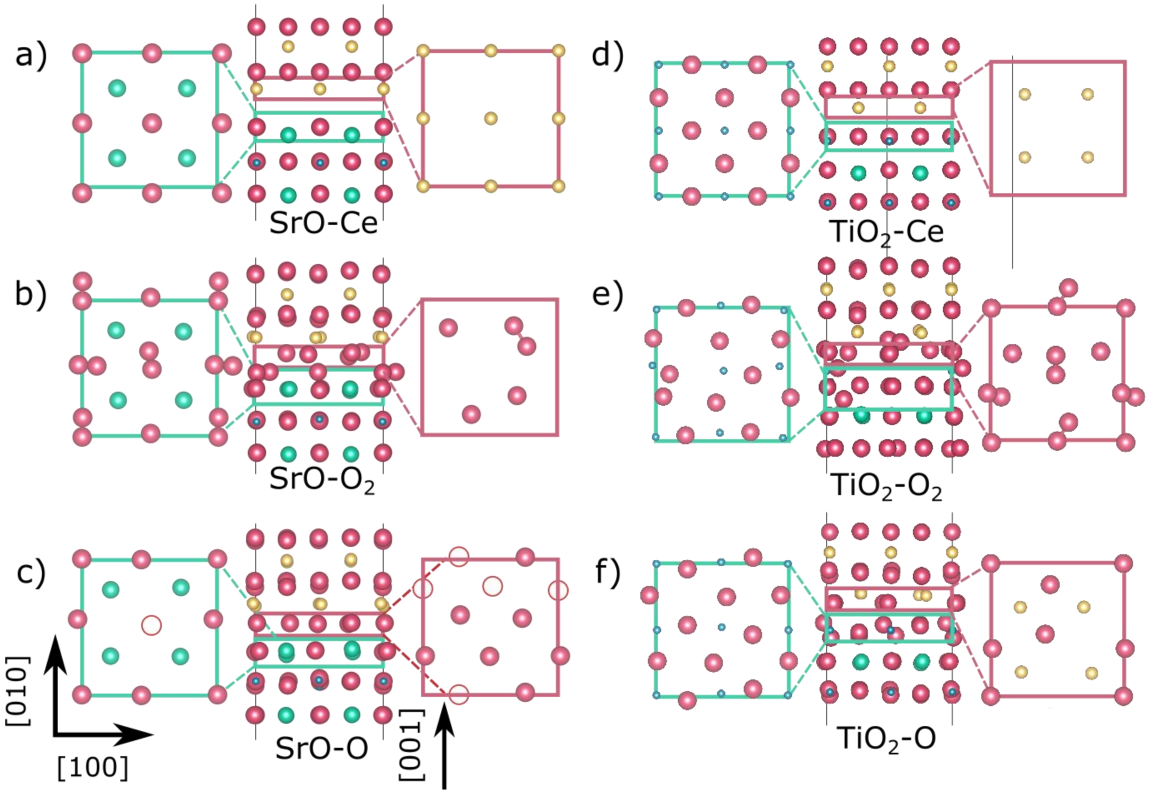

Figure 2. SrO (a-c) and TiO_2 (d-e) terminated interfaces viewed down the [010] direction (center), and down the [001] direction. The interface types are: a) SrO-Ce, b) SrO-O_2, and c) SrO-O, d) TiO_2-Ce, e) TiO_2-O_2, f) TiO_2-O. Color coding: Sr-green, Ti-blue, Ce-yellow, O-Red.

The lowest energy structure found for the SrO-O type termination is shown in Figure 2c. Apart from the existence of vacant oxygen sites, shown as hollow red circles, the atomic arrangement in the interface layers appear to follow that of the bulk phase (as in Figure 1). There are three empty sites in the O_2 layer and the other one is inside the SrO layer. We will come back to discuss the implications of these vacancies later.

Structures found for TiO_2 terminated STO are shown in Figure 2d-f. The TiO_2-Ce structure (Figure 2d) has little reconstruction at the interface. Also, the oxygen sub-lattice in the TiO_2 layer is identical to that in bulk CeO_2, which maintains 8-fold coordination environments of Ce atoms at the interface. The existence of Ti^{4+} in the same layer, however, causes the inter-layer distance to increase through electrostatic repulsion. Similar to the SrO-O_2 termination of Figure 2b, peroxide groups exist also in the structure with the TiO_2-O_2 termination, as shown in Figure 2e. The TiO_2-O interface contains a buckled rock salt ordered CeO layer at the interface (Figure 2f).

The buckling is caused by the relatively small ionic radius of Ce^{4+} as well as the repulsion from the O_2 layer above.

Terminations and stability

Relative stability of the interface models mentioned above can be compared via interface excess energy as a function of oxygen chemical potential (see SI for more details). In Figure 3, the difference in excess energy per unit area ($d\sigma$) is plotted against the oxygen chemical potential ($\mu_O' = \mu_O - \mu_O^0$) for both SrO and TiO_2 terminations, where n_O labels the relative oxygen contents. Only the lowest energy structures for each composition are included. At the oxygen deficient limit, i.e. when μ_O' is highly negative, the SrO-Ce and TiO_2-Ce ($n_O = -4$) configurations are stable. Similarly, the SrO-O_2 and TiO_2-O_2 ($n_O = 4$) cases are stable at the oxygen rich limit. The SrO-O and TiO_2-O interfaces are stable under intermediate condition and have $n_O = 0$ as indicated by the black lines in Figure 3. Other compositions with n_O between +4 and -4 are also included. Using the thermodynamic data of molecular oxygen, a phase diagram can be constructed (Figure S1). Both SrO-O and TiO_2-O structures are found to be stable under typical film deposition conditions. Their structural parameters including the lattice constants and bond lengths are summarized in Table S3. The calculated projected density of states and band structures suggest the two interfaces remain electronically insulating (Figure S2-4). A shift of the conduction band minimum/valence band maximum can be seen in the layer-by-layer projected density of state, which can be related to the difference in the band gaps and electrostatic potential between $SrTiO_3$ and CeO_2. Semiconductor band bending at heterointerface is known to affect the electronic conductivity in other ionic conductor systems[47,48]. Interfaces with other terminations may become conductive as the Fermi level moves into the conduction band or the valence band as shown in Figure S5-6.

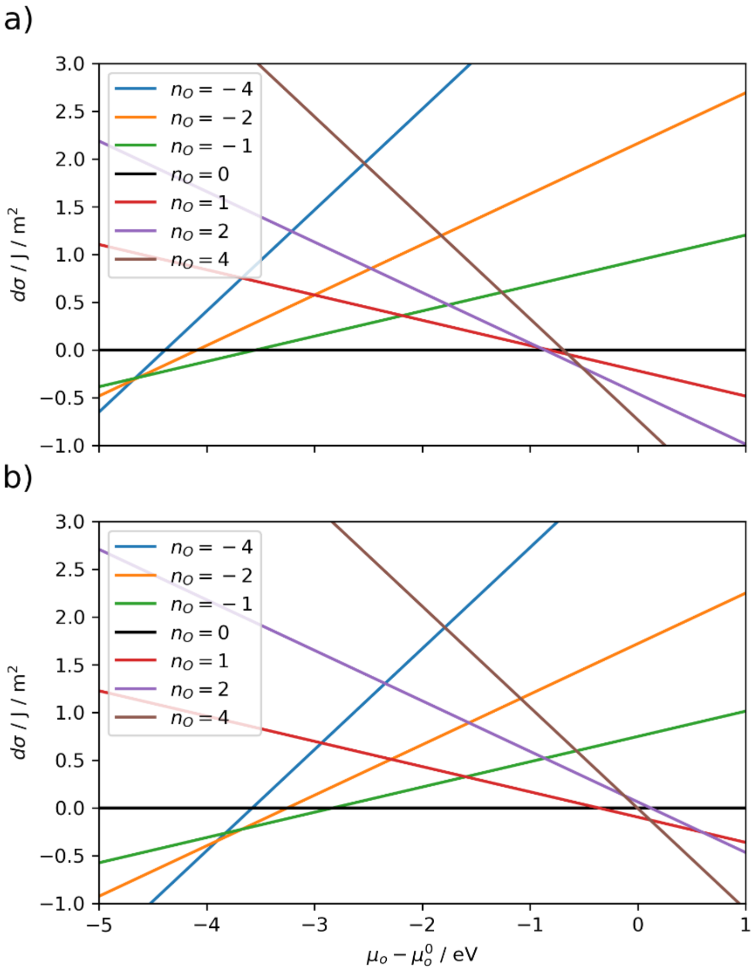

Figure 3. Stability of the interfaces. Relative stability plot for (a) SrO and (b) TiO_2 terminated interface structures with different oxygen stoichiometry.

Vacancy formation energies

Having resolved the atomic structures at the interface, we now turn our focus to the properties they give rise to. The transport of oxygen ions in CeO_2 relies on the existence of oxygen vacancies. Vacancy formation energies at various sites at the SrO-O (Figure 2c) and TiO_2-O (Figure 2f) interface structures are shown in Figure 4. The lowest vacancy formation energy in each layer plotted against their *z* coordinates. Note that only the relative values are of the interest (Figure S7) here rather than the absolute vacancy formation energy which will require larger supercell to converge[49]. At the SrO-O interface, the formation energy is reduced from the bulk CeO_2 value of 3.0 eV down to 2.3 eV. The decrease is more prominent in the TiO_2-O structure, where the formation energy decreases to 1.5 eV at the interface and the reduction penetrates the CeO_2 layers deeper. It was found that vacancies initially placed in the adjacent STO layer can automatically migrate to the interface during the geometry optimisation.

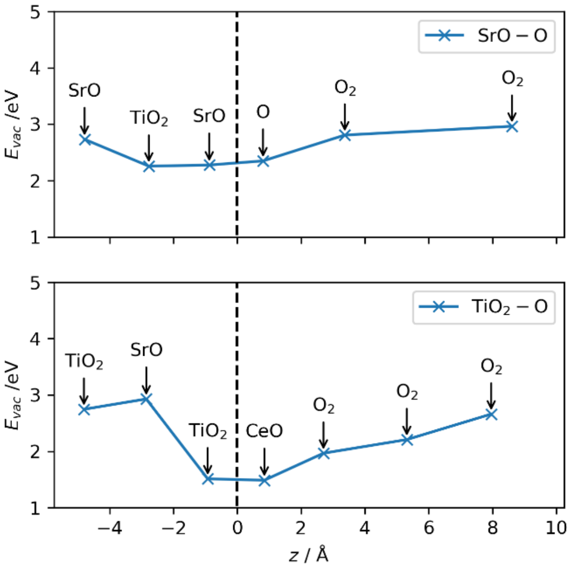

Figure 4. Formation energy of oxygen vacancies. Oxygen vacancy formation energies plotted against z (parallel to the [001] direction) at the SrO-O and TiO_2-O interfaces. Structures shown in Figure 2c&f are used for the computation. The interface is marked by the dotted line, and $z = 0$ corresponds to the location of the interface.

Ionic diffusivity

Ionic diffusivity can be strongly affected by the atomic structures and their corresponding energy landscapes. Unoccupied oxygen sites (i.e. oxygen vacancies) can potentially enhance diffusivity at the interface, which otherwise relies on intrinsic oxygen vacancies that are fewer in number in undoped material, giving poor ionic conductivities ($\sim 3.13 \times 10^{-3}$ S /cm at 1000 °C).[50] We carried out molecular dynamics (MD) simulations to investigate oxygen diffusion at the interface based on the predicted the SrO-O interface structure (Figure 2c). Without explicitly introducing additional vacancies, the oxygen ions are found to be mobile in the lateral directions. Their trajectories within a period of 500 ps at 1600 K (Figure S8). Diffusion is found to be confined within two oxygen layers from the interface on each side. It is evident that such behaviour is strongly related to the interface reconstruction causing partially occupied oxygen sites. In addition, the lack of vacancy movement in the bulk region is consistent with the vacancy formation energy being reduced the interface as discussed above. On the other hand, no long-range diffusion at the TiO_2-O interface has been found using the same simulation settings.

Oxygen diffusivity at 1000 K is estimated by extrapolating the fitted line in Figure S8, giving a value of 1.7×10^{-8} cm^2 / s. The activation energy of 0.52 eV at lower temperatures is similar to those reported for doped-CeO_2, which range from 0.50 eV to 0.75 eV.[51–54] Tensile strain is known to reduce the activation energy, and reductions of around ~0.05 eV based on theoretical studies have been reported for CeO_2 about 2% tensile strain.[21,51] Pristine CeO_2 is expected to have low diffusivity ($\sim 1.0 \times 10^{-10}$ cm^2 / s)[55,56] due to the scarcity of oxygen vacancies as intrinsic defects, and here the interface gives rise to an enhancement of about two orders of magnitude. Repeating the MD simulations using Gd-doped CeO_2 (10% at.) shows that the diffusivity at the interface region has the same order of magnitude compared to bulk GDC (Figure S9). This suggests that similar interfaces in doped/reduced CeO_2[52,57] and YSZ[22] would have very limited effects on enhancing the overall oxygen diffusivity, as the bulk region is already highly ionically conductive.

Experimental verification

To verify the predicted interface structures, epitaxial thin films of CeO_2 were grown on STO (001) substrates using pulsed-laser deposition and subsequently characterized under scanning transmission electron microscopy (STEM). Samples with both TiO_2 and SrO termination were prepared, as described in the SI, where results of film quality and surface morphology characterizations are also displayed (Figure S13-S17). STEM is capable of imaging individual columns of atoms with multiple imaging modes. High-angle annular dark field (HAADF) images (Figure 5a&c) are used to reveal the positions of the metal cations, since it is based on "Z-contrast".[8,58] The annular bright field (ABF) images (Figure 5b&d) are less Z-dependent, allowing the oxygen anion positions to be revealed, which are left out by the HAADF images.

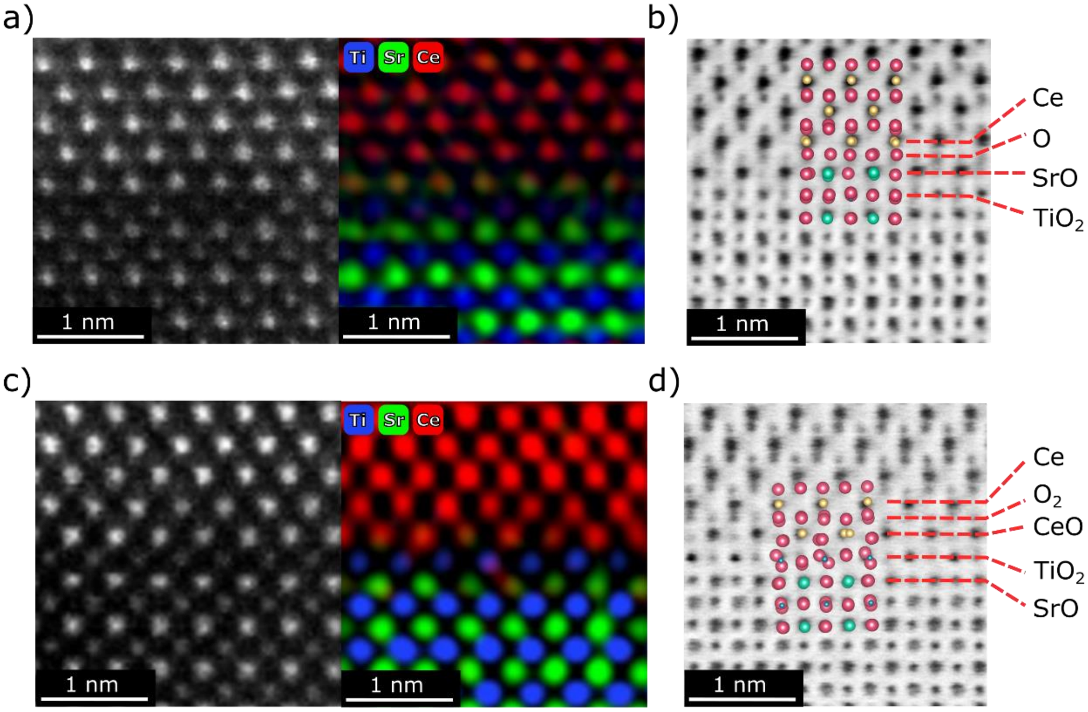

Figure 5. Scanning transmission electron microscopy images of the CeO_2-STO interface in PLD-grown films of CeO_2 on STO single crystal substrates, where the STO has a SrO (a, b) and a TiO_2 (c, d) termination. The dark field images are shown side-by-side with the energy dispersive X-ray spectrometry (EDS) elemental maps in a) and c), which verify the designed terminations on the $SrTiO_3$ side. In the ABF images b) and d), the predicted interface structures (Figure 2c&f), are overlayed on the annular bright field images. Color coding: Sr-green, Ti-blue, Ce-yellow, O-Red.

The experimentally observed interfaces match well with the predictions. In Figure 5a, the HAADF and elemental energy dispersive X-ray spectrometry (EDS) maps of the SrO terminated sample confirm the SrO termination, but the maps also indicate that the terminal SrO layer may exhibits some Ce/Sr intermixing (see SI for more). The ABF images for both SrO and TiO_2-terminated samples are shown in Figure 5b and Figure 5d respectively, with the corresponding SrO/TiO_2-O interface models overlaid (Figure 2c&f). The assignment of layer identities is assisted with the HAADF and EDS data. In the ABF images of the SrO terminated sample, columns of atoms appear as dark dots, allowing the region of $SrTiO_3$ and CeO_2 to be identified. At the interface, an extra layer of dark dots (labeled "O" in Figure 5b) appears in a similar arrangement as the oxygen layer in CeO_2, but its intensity is decreased. This feature is consistent with the prediction of a partially occupied oxygen layer in the SrO-O model. Although ABF cannot unambiguously differentiate between a fully occupied and a partially occupied O layer, our DFT calculations have shown that a fully occupied layer is not stable. The latter also results in oxygen anions moving off the lattice site (Figure 2b), which is not found in the ABF image, nor is any oxygen dumbbell structure.

For the TiO_2 terminated interface, oxygen anions inside the terminal CeO layer can be clearly seen in the ABF image in Figure 5d (labeled "CeO") as smaller dark dots. In addition, they are displaced towards the STO side, which is consistent with the interface model in Figure 2f. Overall, the STEM images provide an invaluable support on the validity of our predictions of the interface structures and the calculated stabilities. The experimental results therefore underpin our calculation results on oxygen vacancy formation energy and diffusivity.

Discussion

Variation of the local composition has been suggested as the key to stabilizing interfaces[5,29,59]. Dyer et al.[29] studied the YSZ-STO interface by locally optimizing a range of hand-built models. It was reported that under the oxygen rich limit an interface containing a rock salt structured ZrO layer ($n_O = 0$) has lower excess energy compared to that with O_2 ($n_O = 4$) or Zr ($n_O = -4$) termination. Our results here, obtained via structure searching without any *a priori* model, suggest that at the O-rich limit ($\mu'_O = 0$ eV) the stable structures contain peroxide groups (dumbbells, Figure 2b&e). The ionic interface reconstructions here can be seen as responding to both structural and chemical mismatches between the two materials, in analogy to the electronic reconstruction at the $SrTiO_3$/$LaAlO_3$ interface giving rise to a 2D electron gas. Modelling interfaces are computational challenging due to model size and complexities arise from local minima, choices of terminations, lateral alignment and systematic errors in the lattice parameters. Finding low energy configurations through structure searching is particularly useful, but the limit in model sizes and other approximations used still require careful convergence. Further works need to use large cell sizes with the help machine learning potentials which have gained significant improvements in recent years[60–63].

Interfaces and grain boundaries are known to act as sinks of defects in ceramic materials. However, direct measurement of defect concentrations at interfaces is challenging and often limited to model systems. The effect of interfaces on vacancy stability has been reported in several theoretical works, but so far has been limited to interfaces between the same structure type[42] or has relied on hand-built models.[64,65] The accumulation of vacancies at the STO-CeO_2 interface may enhance the oxygen transport along the interface, but conduction is likely to be hindered perpendicular to the interface. This is because vacancies moving away from the interface requires additional energy. A space charge region would be present if the intrinsic concentration of the oxygen vacancies is low, i.e. when the CeO_2 is undoped. Such a region is expected to extend much further into CeO_2. A previous study on the Y_2O_3/CeO_2 interface has estimated a Debye length of 3 nm, creating a zone of increased oxygen vacancy concentration around 10 nm which can enhance the ionic conductivity[66]. Our study shows that the interface terminations also play a role here. The TiO_2-O terminated interface has a large reduction in the oxygen vacancy formation energy, which would result in stronger space charge effects.

The stable SrO-O interface structure (Figure 2c) contains many unoccupied oxygen sites (depicted by the empty circles). Dopants such as trivalent Sm or Gd, are known to induce charge compensation vacancies in CeO_2, and thereby enhance the ionic diffusivity (and hence the conductivity). In analogy, a SrO termination layer may be seen as localized dopants which induces the vacancies. When half of the Ce^{4+} atoms are replaced by Sr^{2+} in CeO_2, one in four oxygen sites should be vacant to balance the charge. Conversely, the lack of additional oxygen vacancies at a TiO_2 terminated interface (Figure 2f) can be attributed to Ti and Ce having the same +4 oxidation state. Similar results of interface induced oxygen vacancies have been reported in CeO_2/Y_2O_3 nanobrush structures where well-defined (111) interfaces are formed[67]. It was reported that more than 10% of the oxygen atoms are removed at the interface without inducing structural deterioration.

Previous theoretical and computational studies on strain-induced enhancement of oxygen diffusivity in fluorite-structured ionic conductors have shown that tensile strain increases the oxygen diffusivity by modifying the activation energy.[19–21,46,68] The estimated enhancement is limited to at most four-orders of magnitude (at 500 K) with a 4% tensile strain.[21] In fact, excessive tensile strain may even reduce the diffusivity[46] and stabilize alternative phases of YSZ.[22,42,69] Most of these studies have adopted bulk structure models rather than explicitly including the interface, neglecting the apparent strong mismatch in crystal structure between the fluorite/perovskite interface. Here, we fill the missing piece in by explicitly searching reconstructed interface structure that are low in energy.

Our results show that even with an emerging partially occupied oxygen sublattice localized at the interface, the magnitude of the resulting diffusivity is enhanced to a level similar to other doped fluorite conductors. Doped CeO_2 already has many oxygen vacancies, and so any extra vacancies from the interface reconstruction are unlikely to give rise to further increases of the oxygen diffusivity.

Conclusion

In summary, we undertook a systematic search for stable STO/CeO_2 interfaces using AIRSS. The obtained interface models were validated by the STEM images, and allowed the effect of interfaces on the ionic conductivity to be determined. Structural and chemical mismatching between STO and CeO_2 was found to induce localized atomistic reconstructions, resulting in unoccupied oxygen sites when the STO was terminated by a SrO layer. MD simulations showed lateral oxygen ion diffusion localized at the interface, and the calculated diffusivity was found to be 1.7×10^{-8} cm^2 / s at 1000 K, which is only a moderate enhancement from the bulk value, and is similar to that achieved in doped ceria. In fact, the interface itself acts as a region of localized aliovalent Sr^{2+} doping. On the other hand, when STO is terminated by TiO_2, the reconstructed interface contains a rock salt ordered CeO layer without any oxygen vacancies or any enhanced ionic conduction. For both terminations, additional oxygen vacancies are expected to be attracted to the interface which is detrimental to ionic transport perpendicular to the interface. While reconstructions can lead to locally enhanced ionic conductivity, which may have profound effects in nanoionics systems, its effect is limited when the materials are already bulk ionic conductors. Hence, we conclude the combined effect of interface structure and strain cannot lead to the eight orders of magnitude increase in ionic conductivity previously reported at YSZ/STO interface[12]. More broadly, our work shows that computational interface structure searching combined with STEM analysis provide an invaluable tool combination for modelling and understanding non-trivial heterogeneous interfaces, which are not possible to obtain otherwise due to the lack of reliable atomistic models.

Methods

Structure searching and DFT calculations

A detailed discussion about AIRSS, and its applications to interfaces can be found in the literature.[33,39,43,70,71] Briefly, random but physically sensible interface structures are generated and relaxed to their nearby local minimum. The randomly generated structures are relaxed using standard DFT calculations without constraints and these relaxed structures are ranked by their energy. The process is repeated until sets of low energy structures are encountered multiple times. We impose bulk-like species-pair minimum distances constraints in the initial structure generation to limit the search space. Atoms within a single bulk (001) plane on each side of the interface are randomized. We also tested searches with an extended randomization zone up to two layers from each side but found no additional lower energy structures. The lateral alignment between the STO and CeO_2 is varied during generation. No constraints are applied during local optimization, which allows the interface to drive the system into the optimum alignment. A slab cell construction with 15 Å vacuum is used for the initial search. The supercell contains $2 \times 2 \times 2$ primitive cells of STO, with the bottom-most layer is fixed to the bulk coordinates. Two unit cells of bulk CeO_2 are placed on top of the STO block. Half of the oxygen at the top CeO_2(001) surface are removed according to experimentally observed surface reconstructions.[72] To compare relative stability between different stoichiometries and avoid inclusion of surfaces the structures are converted into dual-interface models. This is possible because both STO and CeO_2 have mirror planes parallel to (001) planes.

Density functional theory (DFT) calculations are performed using the plane-wave pseudopotential package CASTEP.[73] Generalized gradient approximation (GGA) based exchange-correlation functionals have been used in many other computational studies of STO and CeO_2 and are shown to give consistent results[42,74–77]. We choose to use the PBEsol[78] exchange-correlation functional since it gives lattice parameters closer to the experimental values for both STO and CeO_2. The valence states $2s^2\ 2p^4$ for O, the $3s^2\ 2p^6\ 3d^2\ 4s^2$ states for Ti, the $4s^2\ 4p^6\ 5s^2$ states for Sr and the $4f^1\ 5s^2\ 5p^6\ 5d^1\ 6s^2$ states for Ce are treated using on-the-fly generated core-corrected ultrasoft pseudopotentials from library QC5. A cut-off energy of 300 eV for the plane wave basis set is used in conjunction with soft pseudopotentials for initial searching, and a $2 \times 2 \times 1$ k-point grid is used. Higher quality pseudopotentials (from library C9) are used for subsequent investigations with a cut-off energy of 600 eV and a $4 \times 4 \times 1$ k-point grid. The one-the-fly generation strings of both sets of pseudopotentials are tabulated in the supplementary material. Since DFT is known to over-bind oxygen molecules (spin-triplet state), a 1.18 eV correction (per O_2) is applied for the oxygen chemical potential reference, obtained by fitting experimental formation energies of alkali and alkaline metal oxides, as described in the literature[79]. Vacancy formation energies and transition state barrier calculation were performed using $\sqrt{2} \times \sqrt{2}$ supercells ($2\sqrt{2} \times 2\sqrt{2}$ of the perovskite primitive cell). We found this supercell size to be sufficient for obtaining relative differences in vacancy formation energies. The Atomic Simulation Environment[80] is used for model construction and conversion. DFT calculations are managed by AiiDA[81] which helps serving the provenance. The AIRSS code version 0.9.1 was used for generating random structures.

Molecular dynamic simulations

Buckingham potentials with long-range Coulomb interactions are used for molecular dynamics simulations performed with LAMMPS.[82] Parameters of the potentials are described in the previous work.[70] Oxygen mean squared displacements (MSDs) are extracted with respect to a range of time origins for averaging..

The simulation box includes 8 × 8 unit cells in the x and y directions with a mirror slab geometry like the DFT calculations, and additional bulk layers have been inserted to increase the separation between the two mirror interfaces. The lattice constants are 31.0Å, 31.0Å and 48.5Å along the x, y and z directions. The simulation includes a total of 3456 atoms and a time step of 2 fs. The NVT ensemble (Nosé–Hoover thermostat) is used with an initial temperature ramping stage of 20 ps. The simulation is then run for 500 ps to sample the MSD. The simulations were repeated for at least eight times for each temperature to provide adequate statistics.

Experimental

TiO_2-terminated STO (001) substrates were used for growing CeO_2 films from the chemically stoichiometric CeO_2 ceramic targets by using a KrF excimer laser (248 nm) at a laser fluence of 2 J cm^{-2}. The growth temperature of 550 ^oC and oxygen partial pressure of 20 mTorr were used during the deposition. The termination of STO from TiO_2 to SrO was achieved by using a $SrRuO_3$ target to deposit an ultrathin layer monitored using reflective high energy electron diffraction (RHEED). Because the RuO_2 layer is highly volatile, the film is self-terminated with the SrO surface afterwards.[83] This process was carried out at 700 ^oC in 100 mTorr oxygen partial pressure and at a laser fluence of 1 J cm^{-2}. After growth, the films were cooled down to room temperature under an oxygen pressure of 20 mTorr. Electron microscopy analysis carried out afterwards confirms the absence of any residual RuO_2, which otherwise may affect the interface properties.[84] Film structures and surface morphologies were investigated by X-ray diffraction (XRD) on a high-resolution X-ray diffractometer (Empyrean, PANalytical, The Netherlands) using Cu K_α radiation (λ = 1.5405 Å) and atomic force microscopy (AFM), respectively.

Cross-sectional samples for STEM measurements were prepared using a focused ion beam (FIB) instrument. The high-angle annular dark field (HAADF) and annular bright field (ABF) images were acquired on a probe corrected STEM (FEI Titan Cubed Themis 60-300) operated at 300 kV. The collection angle range of the HAADF detector was 64~200 mrad, while the collection angle range of ABF images was calibrated at 8~53 mrad, acquired with a DF2 detector.

Acknowledgments

B.Z. acknowledges support from China Scholarship Council and Cambridge Commonwealth, European and International Trust. This study was supported by the Beijing Institute of Technology Research Fund Program for Young Scholars. C.J.P. was supported by the Royal Society through a Royal Society Wolfson Research Merit award. G.S. acknowledges support from EPSRC Grant No. EP/J010863/2. W.-W.L. and J.L.M.-D. acknowledge support from EPSRC Grant EP/L011700/1, EP/N004272/1, EP/P007767/1, and the Isaac Newton Trust (Minute 13.38(k)). J.L.M.-D. acknowledges support from the Royal Academy of Engineering (Grant No. CiET1819_24), the H2020-FETPROACT-2020-2 grant EPISTORE, 10101017709, and the ERC grant, EU-H2020-ERC-ADG # 882929. This work was also supported by Basic Science Center Project of NSFC (51788104) and National Natural Science Foundation of China (51525102). In this work we used the resources of the National Center for Electron Microscopy in Beijing and Shanghai Supercomputer Center. W.-W.L. acknowledges support from the National Natural Science Foundation of China (Grant No. 52102177), the National Natural Science Foundation of Jiangsu Province (Grant No. BK20210313), and Top-notch Academic Programs Project of Jiangsu Higher Education Institutions (TAPP). W.-W.L. also acknowledges the support from the Fundamental Research Funds for the Central Universities (Grant No. NS2023057 and NI2023001) and the support from the Jiangsu Specially-Appointed Professor Program. The research work is supported by the supporting funds for talents of Nanjing University of Aeronautics and Astronautics. This work is supported by Beijing Institute of Technology Research Fund Program for Young Scholars.

We are grateful for computational support from the UK national high performance computing service, ARCHER, and UK Materials and Molecular Modelling Hub (partially funded by EPSRC EP/P020194), for which access was obtained via the UKCP consortium and funded by EPSRC grant ref EP/P022561/1. We are also grateful for computational support from the Cambridge Service for Data Driven Discovery (CSD3) operated by the University of Cambridge Research Computing Service (www.csd3.cam.ac.uk), provided by Dell EMC and Intel using Tier-2 funding from the Engineering and Physical Sciences Research Council (capital grant EP/P020259/1), and DiRAC funding from the Science and Technology Facilities Council (www.dirac.ac.uk).

Supplementary Material

See the supplementary material for additional figures of molecular dynamics simulations, projected electronic density of states, electronic band structure, transition state barrier calculations, phase diagram, testing supercell size for vacancy formation energies; discussions about interface mixing, tables of the pseudopotentials used and structural parameters of interface models.

Data Availability Statement

The data that support the findings of this study are available from the corresponding author upon reasonable request.

Author Declarations

The authors have no conflicts to disclose.

References

(1) J. L. MacManus-Driscoll, J.; Wu, R.; Li, W. Interface-Related Phenomena in Epitaxial Complex Oxide Ferroics across Different Thin Film Platforms: Opportunities and Challenges. *Materials Horizons* **2023**, *10* (4), 1060–1086. https://doi.org/10.1039/D2MH01527G.

(2) Li, W.; Shi, J.; Zhang, K. H. L.; MacManus-Driscoll, J. L. Defects in Complex Oxide Thin Films for Electronics and Energy Applications: Challenges and Opportunities. *Mater. Horiz.* **2020**, *7* (11), 2832–2859. https://doi.org/10.1039/D0MH00899K.

(3) Chakhalian, J.; Millis, A. J.; Rondinelli, J. Whither the Oxide Interface. *Nature Mater* **2012**, *11* (2), 92–94. https://doi.org/10.1038/nmat3225.

(4) Hwang, H. Y.; Iwasa, Y.; Kawasaki, M.; Keimer, B.; Nagaosa, N.; Tokura, Y. Emergent Phenomena at Oxide Interfaces. *Nat Mater* **2012**, *11* (2), 103–113. https://doi.org/10.1038/nmat3223.

(5) Leon, C.; Santamaria, J.; Boukamp, B. A. Oxide Interfaces with Enhanced Ion Conductivity. *MRS Bulletin* **2013**, *38* (12), 1056–1063. https://doi.org/10.1557/mrs.2013.264.

(6) Ohtomo, A.; Hwang, H. Y. A High-Mobility Electron Gas at the LaAlO3/SrTiO3 Heterointerface. *Nature* **2004**, *427* (6973), 423–426. https://doi.org/10.1038/nature02308.

(7) Michaeli, K.; Potter, A. C.; Lee, P. A. Superconducting and Ferromagnetic Phases in {${\mathrm{SrTiO}}_{3}/{\mathrm{LaAlO}}_{3}$ }Oxide Interface Structures: Possibility of Finite Momentum Pairing. *Phys. Rev. Lett.* **2012**, *108* (11), 117003. https://doi.org/10.1103/PhysRevLett.108.117003.

(8) Li, W.; Zhu, B.; Zhu, R.; Wang, Q.; Lu, P.; Sun, Y.; Cafolla, C.; Qi, Z.; Chen, A.; Gao, P.; Wang, H.; He, Q.; Zhang, K. H. L.; MacManus-Driscoll, J. L. Atomic-Scale Control of Electronic Structure and Ferromagnetic Insulating State in Perovskite Oxide Superlattices by Long-Range Tuning of BO6 Octahedra. *Advanced Functional Materials* **2020**, *30* (40), 2001984. https://doi.org/10.1002/adfm.202001984.

(9) Li, D.; Wang, H.; Li, K.; Zhu, B.; Jiang, K.; Backes, D.; Veiga, L. S. I.; Shi, J.; Roy, P.; Xiao, M.; Chen, A.; Jia, Q.; Lee, T.-L.; Dhesi, S. S.; Scanlon, D. O.; MacManus-Driscoll, J. L.; van Aken, P. A.; Zhang, K. H. L.; Li, W. Emergent and Robust Ferromagnetic-Insulating State in Highly Strained Ferroelastic LaCoO3 Thin Films. *Nat Commun* **2023**, *14* (1), 3638. https://doi.org/10.1038/s41467-023-39369-6.

(10) Gomez, S. Y.; Hotza, D. Current Developments in Reversible Solid Oxide Fuel Cells. *Renewable and Sustainable Energy Reviews* **2016**, *61*, 155–174. https://doi.org/10.1016/j.rser.2016.03.005.

(11) Wachsman, E. D.; Lee, K. T. Lowering the Temperature of Solid Oxide Fuel Cells. *Science* **2011**, *334* (6058), 935–939. https://doi.org/10.1126/science.1204090.

(12) Garcia-Barriocanal, J.; Rivera-Calzada, A.; Varela, M.; Sefrioui, Z.; Iborra, E.; Leon, C.; Pennycook, S. J.; Santamaria, J. Colossal Ionic Conductivity at Interfaces of Epitaxial ZrO2:Y2O3/SrTiO3 Heterostructures. *Science* **2008**, *321* (5889), 676–680. https://doi.org/10.1126/science.1156393.

(13) Pennycook, T. J.; Beck, M. J.; Varga, K.; Varela, M.; Pennycook, S. J.; Pantelides, S. T. Origin of Colossal Ionic Conductivity in Oxide Multilayers: Interface Induced Sublattice Disorder. *Phys. Rev. Lett.* **2010**, *104* (11), 115901. https://doi.org/10.1103/PhysRevLett.104.115901.

(14) Pennycook, T. J.; Oxley, M. P.; Garcia-Barriocanal, J.; Bruno, F. Y.; Leon, C.; Santamaria, J.; Pantelides, S. T.; Varela, M.; Pennycook, S. J. Seeing Oxygen Disorder in YSZ/SrTiO3 Colossal Ionic Conductor Heterostructures Using EELS. *Eur. Phys. J. Appl. Phys.* **2011**, *54* (3), 33507. https://doi.org/10.1051/epjap/2011100413.

(15) Guo, X. Comment on "Colossal Ionic Conductivity at Interfaces of Epitaxial ZrO2:Y2O3/SrTiO3 Heterostructures." *Science* **2009**, *324* (5926), 465–465. https://doi.org/10.1126/science.1168940.

(16) Cavallaro, A.; Burriel, M.; Roqueta, J.; Apostolidis, A.; Bernardi, A.; Tarancón, A.; Srinivasan, R.; Cook, S. N.; Fraser, H. L.; Kilner, J. A.; McComb, D. W.; Santiso, J. Electronic Nature of the Enhanced Conductivity in YSZ-STO Multilayers Deposited by PLD. *Solid State Ionics* **2010**, *181* (13–14), 592–601. https://doi.org/10.1016/j.ssi.2010.03.014.

(17) Souza, R. A. D.; Ramadan, A. H. H. Ionic Conduction in the SrTiO3|YSZ|SrTiO3 Heterostructure. *Phys. Chem. Chem. Phys.* **2013**, *15* (13), 4505–4509. https://doi.org/10.1039/C3CP44399J.

(18) Sillassen, M.; Eklund, P.; Pryds, N.; Johnson, E.; Helmersson, U.; Bøttiger, J. Low-Temperature Superionic Conductivity in Strained Yttria-Stabilized Zirconia. *Advanced Functional Materials* **2010**, *20* (13), 2071–2076. https://doi.org/10.1002/adfm.201000071.

(19) Yildiz, B. "Stretching" the Energy Landscape of Oxides—Effects on Electrocatalysis and Diffusion. *MRS Bulletin* **2014**, *39* (2), 147–156. https://doi.org/10.1557/mrs.2014.8.

(20) Kushima, A.; Yildiz, B. Oxygen Ion Diffusivity in Strained Yttria Stabilized Zirconia: Where Is the Fastest Strain? *Journal of Materials Chemistry* **2010**, *20* (23), 4809–4809. https://doi.org/10.1039/c000259c.

(21) Souza, R. A. D.; Ramadan, A.; Hörner, S. Modifying the Barriers for Oxygen-Vacancy Migration in Fluorite-Structured CeO2 Electrolytes through Strain: A Computer Simulation Study. *Energy Environ. Sci.* **2012**, *5* (1), 5445–5453. https://doi.org/10.1039/C2EE02508F.

(22) Oka, M.; Kamisaka, H.; Fukumura, T.; Hasegawa, T. DFT-Based Ab Initio MD Simulation of the Ionic Conduction in Doped ZrO2 Systems under Epitaxial Strain. *Phys. Chem. Chem. Phys.* **2015**, *17* (43), 29057–29063. https://doi.org/10.1039/C5CP03238E.

(23) Peters, A.; Korte, C.; Hesse, D.; Zakharov, N.; Janek, J. Ionic Conductivity and Activation Energy for Oxygen Ion Transport in Superlattices — The Multilayer System CSZ (ZrO2+CaO)/Al2O3. *Solid State Ionics* **2007**, *178* (1), 67–76. https://doi.org/10.1016/j.ssi.2006.12.004.

(24) Korte, C.; Schichtel, N.; Hesse, D.; Janek, J. Influence of Interface Structure on Mass Transport in Phase Boundaries between Different Ionic Materials. *Monatsh Chem* **2009**, *140* (9), 1069–1080. https://doi.org/10.1007/s00706-009-0125-7.

(25) Pergolesi, D.; Fabbri, E.; Cook, S. N.; Roddatis, V.; Traversa, E.; Kilner, J. A. Tensile Lattice Distortion Does Not Affect Oxygen Transport in Yttria-Stabilized Zirconia–CeO2 Heterointerfaces. *ACS Nano* **2012**, *6* (12), 10524–10534. https://doi.org/10.1021/nn302812m.

(26) Pergolesi, D.; Gilardi, E.; Fabbri, E.; Roddatis, V.; Harrington, G. F.; Lippert, T.; Kilner, J. A.; Traversa, E. Interface Effects on the Ionic Conductivity of Doped Ceria–Yttria-Stabilized Zirconia Heterostructures. *ACS Appl. Mater. Interfaces* **2018**, *10* (16), 14160–14169. https://doi.org/10.1021/acsami.8b01903.

(27) Sun, L.; Marrocchelli, D.; Yildiz, B. Edge Dislocation Slows down Oxide Ion Diffusion in Doped CeO_2 by Segregation of Charged Defects. *Nature Communications* **2015**, *6*, ncomms7294. https://doi.org/10.1038/ncomms7294.

(28) Shi, Q.; Zhong, H.; Huang, M.; Zhu, B.; Huang, L.; Wu, Y. Fast Ionic Transport in SrTiO3/LaAlO3 Heterostructure. *Chem. Commun.* **2022**, *58* (100), 13919–13922. https://doi.org/10.1039/D2CC05205A.

(29) Dyer, M. S.; Darling, G. R.; Claridge, J. B.; Rosseinsky, M. J. Chemical Bonding and Atomic Structure in Y2O3:ZrO2-SrTiO3 Layered Heterostructures. *Angew. Chem. Int. Ed.* **2012**, *51* (14), 3418–3422. https://doi.org/10.1002/anie.201108068.

(30) Cheah, W. L.; Finnis, M. W. Structure of Multilayer ZrO2/SrTiO3. *J. Mater. Sci.* **2012**, *47* (4), 1631–1640. https://doi.org/10.1007/s10853-011-5985-7.

(31) Cheah, W. L.; McComb, D. W.; Finnis, M. W. Structure and Ionic Diffusivity in an Yttria-Stabilised Zirconia/Strontium Titanate Multilayer. *Acta Materialia* **2017**, *129*, 388–397. https://doi.org/10.1016/j.actamat.2017.02.073.

(32) Oganov, A. R.; Pickard, C. J.; Zhu, Q.; Needs, R. J. Structure Prediction Drives Materials Discovery. *Nature Reviews Materials* **2019**, *4* (5), 331. https://doi.org/10.1038/s41578-019-0101-8.

(33) Pickard, C. J.; Needs, R. J. Ab Initio Random Structure Searching. *Journal of physics. Condensed matter : an Institute of Physics journal* **2011**, *23* (5), 053201–053201. https://doi.org/10.1088/0953-8984/23/5/053201.

(34) Wang, Y.; Lv, J.; Zhu, L.; Ma, Y. CALYPSO: A Method for Crystal Structure Prediction. *Computer Physics Communications* **2012**, *183* (10), 2063–2070. https://doi.org/10.1016/j.cpc.2012.05.008.

(35) Oganov, A. R.; Lyakhov, A. O.; Valle, M. How Evolutionary Crystal Structure Prediction Works—and Why. *Acc. Chem. Res.* **2011**, *44* (3), 227–237. https://doi.org/10.1021/ar1001318.

(36) Pickard, C. J.; Needs, R. J. Structure of Phase III of Solid Hydrogen. *Nat Phys* **2007**, *3* (7), 473–476. https://doi.org/10.1038/nphys625.

(37) Morris, A. J.; Pickard, C. J.; Needs, R. J. Hydrogen/Nitrogen/Oxygen Defect Complexes in Silicon from Computational Searches. *Phys. Rev. B* **2009**, *80* (14), 144112. https://doi.org/10.1103/PhysRevB.80.144112.

(38) Chen, J.; Schusteritsch, G.; Pickard, C. J.; Salzmann, C. G.; Michaelides, A. Two Dimensional Ice from First Principles: Structures and Phase Transitions. *Phys. Rev. Lett.* **2016**, *116* (2), 025501. https://doi.org/10.1103/PhysRevLett.116.025501.

(39) Schusteritsch, G.; Pickard, C. J. Predicting Interface Structures: From SrTiO3 to Graphene. *Physical Review B - Condensed Matter and Materials Physics* **2014**, *90* (3), 1–7. https://doi.org/10.1103/PhysRevB.90.035424.

(40) Chua, A. L.-S.; Benedek, N. A.; Chen, L.; Finnis, M. W.; Sutton, A. P. A Genetic Algorithm for Predicting the Structures of Interfaces in Multicomponent Systems. *Nat Mater* **2010**, *9* (5), 418–422. https://doi.org/10.1038/nmat2712.

(41) Yahiro, H.; Eguchi, Y.; Eguchi, K.; Arai, H. Oxygen Ion Conductivity of the Ceria-Samarium Oxide System with Fluorite Structure. *J Appl Electrochem* **1988**, *18* (4), 527–531. https://doi.org/10.1007/BF01022246.

(42) Aidhy, D. S.; Liu, B.; Zhang, Y.; Weber, W. J. Strain-Induced Phase and Oxygen-Vacancy Stability in Ionic Interfaces from First-Principles Calculations. *J. Phys. Chem. C* **2014**, *118* (51), 30139–30144. https://doi.org/10.1021/jp507876m.

(43) Pickard, C. J.; Needs, R. J. High-Pressure Phases of Silane. *Phys. Rev. Lett.* **2006**, *97* (4), 045504. https://doi.org/10.1103/PhysRevLett.97.045504.

(44) Tsuda, K.; Tanaka, M. Refinement of Crystal Structure Parameters Using Convergent-Beam Electron Diffraction: The Low-Temperature Phase of SrTiO3. *Acta Cryst A, Acta Cryst Sect A, Acta Crystallogr A, Acta Crystallogr Sect A, Acta Crystallogr A Found Crystallogr, Acta Crystallogr Sect A Found Crystallogr* **1995**, *51* (1), 7–19. https://doi.org/10.1107/S010876739400560X.

(45) Balaji Gopal, C.; García-Melchor, M.; Lee, S. C.; Shi, Y.; Shavorskiy, A.; Monti, M.; Guan, Z.; Sinclair, R.; Bluhm, H.; Vojvodic, A.; Chueh, W. C. Equilibrium Oxygen Storage Capacity of Ultrathin $CeO_{2-\delta}$ Depends Non-Monotonically on Large Biaxial Strain. *Nature Communications* **2017**, *8*, 15360. https://doi.org/10.1038/ncomms15360.

(46) Tarancón, A.; Morata, A. New Insights into the Origin of the Oxide Ionic Diffusion Change in Strained Lattices of Yttria Stabilized Zirconia. *Computational Materials Science* **2015**, *103*, 206–215. https://doi.org/10.1016/j.commatsci.2014.12.002.

(47) M.A.K. Yousaf Shah; Yuzheng Lu; Naveed Mushtaq; Manish Singh; Sajid Rauf; Muhammad Yousaf; Bin Zhu. ZnO/MgZnO Heterostructure Membrane with Type II Band Alignment for Ceramic Fuel Cells. *Energy Materials* **2022**, *2* (4), 200031. https://doi.org/10.20517/energymater.2022.27.

(48) Shah, M. A. K. Y.; Lu, Y.; Mushtaq, N.; Yousaf, M.; Akbar, N.; Xia, C.; Yun, S.; Zhu, B. Semiconductor-Membrane Fuel Cell (SMFC) for Renewable Energy Technology. *Renewable and Sustainable Energy Reviews* **2023**, *185*, 113639. https://doi.org/10.1016/j.rser.2023.113639.

(49) Buban, J. P.; Iddir, H.; Öğüt, S. Structural and Electronic Properties of Oxygen Vacancies in Cubic and Antiferrodistortive Phases of ${\mathrm{SrTiO}}_{3}$. *Phys. Rev. B* **2004**, *69* (18), 180102. https://doi.org/10.1103/PhysRevB.69.180102.

(50) Basu, S.; Devi, P. S.; Maiti, H. S. Synthesis and Properties of Nanocrystalline Ceria Powders. *Journal of Materials Research* **2004**, *19* (11), 3162–3171. https://doi.org/10.1557/JMR.2004.0442.

(51) Rushton, M. J. D.; Chroneos, A.; Skinner, S. J.; Kilner, J. A.; Grimes, R. W. Effect of Strain on the Oxygen Diffusion in Yttria and Gadolinia Co-Doped Ceria. *Solid State Ionics* **2013**, *230*, 37–42. https://doi.org/10.1016/j.ssi.2012.09.015.

(52) Rushton, M. J. D.; Chroneos, A. Impact of Uniaxial Strain and Doping on Oxygen Diffusion in CeO2. *Scientific reports* **2014**, *4*, 6068–6068. https://doi.org/10.1038/srep06068.

(53) Dholabhai, P. P.; Adams, J. B.; Crozier, P.; Sharma, R. A Density Functional Study of Defect Migration in Gadolinium Doped Ceria. *Phys. Chem. Chem. Phys.* **2010**, *12* (28), 7904–7910. https://doi.org/10.1039/B924534K.

(54) Gotte, A.; Spångberg, D.; Hermansson, K.; Baudin, M. Molecular Dynamics Study of Oxygen Self-Diffusion in Reduced CeO2. *Solid State Ionics* **2007**, *178* (25), 1421–1427. https://doi.org/10.1016/j.ssi.2007.08.003.

(55) Neuderth, P.; Hille, P.; Martí-Sánchez, S.; Mata, M. de la; Coll, M.; Arbiol, J.; Eickhoff, M. Optical Analysis of Oxygen Self-Diffusion in Ultrathin CeO2 Layers at Low Temperatures. *Advanced Energy Materials* **2018**, *8* (29), 1802120. https://doi.org/10.1002/aenm.201802120.

(56) Kamiya, M.; Shimada, E.; Ikuma, Y.; Komatsu, M.; Haneda, H. Intrinsic and Extrinsic Oxygen Diffusion and Surface Exchange Reaction in Cerium Oxide. *J. Electrochem. Soc.* **2000**, *147* (3), 1222. https://doi.org/10.1149/1.1393340.

(57) Cui, Z.; Sun, Y.; Qu, J. Molecular Dynamics Simulation of Reduced CeO2. *Solid State Ionics* **2012**, *226*, 24–29. https://doi.org/10.1016/j.ssi.2012.08.001.

(58) Li, W.; Zhu, B.; He, Q.; Borisevich, A. Y.; Yun, C.; Wu, R.; Lu, P.; Qi, Z.; Wang, Q.; Chen, A.; Wang, H.; Cavill, S. A.; Zhang, K. H. L.; MacManus-Driscoll, J. L. Interface Engineered Room-Temperature Ferromagnetic Insulating State in Ultrathin Manganite Films. *Advanced Science* **2020**, *7* (1), 1901606. https://doi.org/10.1002/advs.201901606.

(59) O'Sullivan, M.; Hadermann, J.; Dyer, M. S.; Turner, S.; Alaria, J.; Manning, T. D.; Abakumov, A. M.; Claridge, J. B.; Rosseinsky, M. J. Interface Control by Chemical and

Dimensional Matching in an Oxide Heterostructure. *Nature Chemistry* **2016**, *8* (4), 347–353. https://doi.org/10.1038/nchem.2441.

(60) Behler, J.; Csányi, G. Machine Learning Potentials for Extended Systems: A Perspective. *Eur. Phys. J. B* **2021**, *94* (7), 142. https://doi.org/10.1140/epjb/s10051-021-00156-1.

(61) Pickard, C. J. Ephemeral Data Derived Potentials for Random Structure Search. *Phys. Rev. B* **2022**, *106* (1), 014102. https://doi.org/10.1103/PhysRevB.106.014102.

(62) Salzbrenner, P. T.; Joo, S. H.; Conway, L. J.; Cooke, P. I. C.; Zhu, B.; Matraszek, M. P.; Witt, W. C.; Pickard, C. J. Developments and Further Applications of Ephemeral Data Derived Potentials. *The Journal of Chemical Physics* **2023**, *159* (14), 144801. https://doi.org/10.1063/5.0158710.

(63) Batzner, S.; Musaelian, A.; Kozinsky, B. Advancing Molecular Simulation with Equivariant Interatomic Potentials. *Nat Rev Phys* **2023**, *5* (8), 437–438. https://doi.org/10.1038/s42254-023-00615-x.

(64) Dholabhai, P. P.; Aguiar, J. A.; Misra, A.; Uberuaga, B. P. Defect Interactions with Stepped CeO2/SrTiO3 Interfaces: Implications for Radiation Damage Evolution and Fast Ion Conduction. *The Journal of Chemical Physics* **2014**, *140* (19), 194701. https://doi.org/10.1063/1.4876225.

(65) Dholabhai, P. P.; Martinez, E.; Brown, N. T.; Uberuaga, B. P. On the Mobility of Carriers at Semi-Coherent Oxide Heterointerfaces. *Phys. Chem. Chem. Phys.* **2017**, *19* (34), 23122–23130. https://doi.org/10.1039/c7cp04884j.

(66) Shen, W.; Jiang, J.; Ni, C.; Voras, Z.; Beebe, T. P.; Hertz, J. L. Two-Dimensional Vacancy Trapping in Yttria Doped Ceria. *Solid State Ionics* **2014**, *255*, 13–20. https://doi.org/10.1016/j.ssi.2013.11.012.

(67) Lee, D.; Gao, X.; Sun, L.; Jee, Y.; Poplawsky, J.; Farmer, T. O.; Fan, L.; Guo, E.-J.; Lu, Q.; Heller, W. T.; Choi, Y.; Haskel, D.; Fitzsimmons, M. R.; Chisholm, M. F.; Huang, K.; Yildiz, B.; Lee, H. N. Colossal Oxygen Vacancy Formation at a Fluorite-Bixbyite Interface. *Nat Commun* **2020**, *11* (1), 1371. https://doi.org/10.1038/s41467-020-15153-8.

(68) Aydin, H.; Korte, C.; Janek, J. 18O-Tracer Diffusion along Nanoscaled Sc2O3/Yttria Stabilized Zirconia (YSZ) Multilayers: On the Influence of Strain. *Science and Technology of Advanced Materials* **2013**, *14* (3), 035007. https://doi.org/10.1088/1468-6996/14/3/035007.

(69) Oka, M.; Kamisaka, H.; Fukumura, T.; Hasegawa, T. Density Functional Theory-Based Ab Initio Molecular Dynamics Simulation of Ionic Conduction in N-/F-Doped ZrO2 under Epitaxial Strain. *Computational Materials Science* **2018**, *154*, 91–96. https://doi.org/10.1016/j.commatsci.2018.07.038.

(70) Zhu, B.; Schusteritsch, G.; Lu, P.; MacManus-Driscoll, J. L.; Pickard. Determining Interface Structures in Vertically Aligned Nanocomposite Films. *APL Materials* **2019**, *7* (6), 061105. https://doi.org/10.1063/1.5099204.

(71) Schusteritsch, G.; Ishikawa, R.; Elmaslmane, A. R.; Inoue, K.; McKenna, K. P.; Ikuhara, Y.; Pickard, C. J. Anataselike Grain Boundary Structure in Rutile Titanium Dioxide. *Nano Lett.* **2021**, *21* (7), 2745–2751. https://doi.org/10.1021/acs.nanolett.0c04564.

(72) Herman, G. S. Characterization of Surface Defects on Epitaxial CeO2(001) Films. *Surface Science* **1999**, *437* (1), 207–214. https://doi.org/10.1016/S0039-6028(99)00723-2.

(73) Clark, S. J.; Segall, M. D.; Pickard, C. J.; Hasnip, P. J.; Probert, M. I. J.; Refson, K.; Payne, M. C. First Principles Methods Using CASTEP. *Zeitschrift für Kristallographie* **2005**, *220* (5-6–2005), 567–570. https://doi.org/10.1524/zkri.220.5.567.65075.

(74) Choi, Y.; Scott, M.; Söhnel, T.; Idriss, H. A DFT + U Computational Study on Stoichiometric and Oxygen Deficient M–CeO2 Systems (M = Pd1, Rh1, Rh10, Pd10 and

Rh4Pd6). *Phys. Chem. Chem. Phys.* **2014**, *16* (41), 22588–22599. https://doi.org/10.1039/C4CP03366C.

(75) Castleton, C. W. M.; Kullgren, J.; Hermansson, K. Tuning LDA+U for Electron Localization and Structure at Oxygen Vacancies in Ceria. *The Journal of Chemical Physics* **2007**, *127* (24), 244704. https://doi.org/10.1063/1.2800015.

(76) Triggiani, L.; B. Muñoz-García, A.; Agostiano, A.; Pavone, M. Promoting Oxygen Vacancy Formation and P-Type Conductivity in SrTiO 3 via Alkali Metal Doping: A First Principles Study. *Physical Chemistry Chemical Physics* **2016**, *18* (41), 28951–28959. https://doi.org/10.1039/C6CP05089A.

(77) Pentcheva, R.; Pickett, W. E. Avoiding the Polarization Catastrophe in LaAlO3 Overlayers on SrTiO3(001) through Polar Distortion. *Physical Review Letters* **2009**, *102* (10), 3–6. https://doi.org/10.1103/PhysRevLett.102.107602.

(78) Perdew, J. P.; Ruzsinszky, A.; Csonka, G. I.; Vydrov, O. A.; Scuseria, G. E.; Constantin, L. A.; Zhou, X.; Burke, K. Restoring the Density-Gradient Expansion for Exchange in Solids and Surfaces. *Phys. Rev. Lett.* **2008**, *100* (13), 136406. https://doi.org/10.1103/PhysRevLett.100.136406.

(79) Wang, L.; Maxisch, T.; Ceder, G. Oxidation Energies of Transition Metal Oxides within the GGA+U Framework. *Phys. Rev. B* **2006**, *73* (19), 195107. https://doi.org/10.1103/PhysRevB.73.195107.

(80) Larsen, A. H.; Mortensen, J. J.; Blomqvist, J.; Castelli, I. E.; Christensen, R.; Marcin Dułak; Friis, J.; Groves, M. N.; Hammer, B.; Hargus, C.; Hermes, E. D.; Jennings, P. C.; Jensen, P. B.; Kermode, J.; Kitchin, J. R.; Kolsbjerg, E. L.; Kubal, J.; Kristen Kaasbjerg; Lysgaard, S.; Maronsson, J. B.; Maxson, T.; Olsen, T.; Pastewka, L.; Andrew Peterson; Rostgaard, C.; Schiøtz, J.; Schütt, O.; Strange, M.; Thygesen, K. S.; Tejs Vegge; Vilhelmsen, L.; Walter, M.; Zeng, Z.; Jacobsen, K. W. The Atomic Simulation Environment—a Python Library for Working with Atoms. *J. Phys.: Condens. Matter* **2017**, *29* (27), 273002. https://doi.org/10.1088/1361-648X/aa680e.

(81) Huber, S. P.; Zoupanos, S.; Uhrin, M.; Talirz, L.; Kahle, L.; Häuselmann, R.; Gresch, D.; Müller, T.; Yakutovich, A. V.; Andersen, C. W.; Ramirez, F. F.; Adorf, C. S.; Gargiulo, F.; Kumbhar, S.; Passaro, E.; Johnston, C.; Merkys, A.; Cepellotti, A.; Mounet, N.; Marzari, N.; Kozinsky, B.; Pizzi, G. AiiDA 1.0, a Scalable Computational Infrastructure for Automated Reproducible Workflows and Data Provenance. *Scientific Data* **2020**, *7* (1), 300. https://doi.org/10.1038/s41597-020-00638-4.

(82) Plimpton, S. Fast Parallel Algorithms for Short-Range Molecular Dynamics. *Journal of Computational Physics* **1995**, *117* (1), 1–19. https://doi.org/10.1006/jcph.1995.1039.

(83) Rijnders, G.; Blank, D. H. A.; Choi, J.; Eom, C.-B. Enhanced Surface Diffusion through Termination Conversion during Epitaxial SrRuO3 Growth. *Appl. Phys. Lett.* **2004**, *84* (4), 505–507. https://doi.org/10.1063/1.1640472.

(84) Akbashev, A. R.; Zhang, L.; Mefford, J. T.; Park, J.; Butz, B.; Luftman, H.; Chueh, W. C.; Vojvodic, A. Activation of Ultrathin SrTiO3 with Subsurface SrRuO3 for the Oxygen Evolution Reaction. *Energy Environ. Sci.* **2018**, *11* (7), 1762–1769. https://doi.org/10.1039/C8EE00210J.